INORGANIC CHEMISTRY FRONTIERS

RESEARCH ARTICLE

View Article Online
View Journal | View Issue



Cite this: *Inorg. Chem. Front.*, 2023, **10**, 5098

# Oxygen vacancies confined in hierarchically porous $CsPbBr_3$@Pb-MOF through *in situ* structural transformation for promoting photocatalytic $CO_2$ reduction†

Yangwen Hou,[a] Man Dong,[c] Jingting He,[a] Jing Sun,[b] Chunyi Sun, *[c] Xiao Li,[b] Xinlong Wang [c] and Zhongmin Su *[b,d]

All-inorganic perovskite ($CsPbBr_3$) nanocrystals (NCs) are exceptional candidates for photocatalysis due to their optimal band structure, high molar extinction coefficient, and long charge-carrier diffusion lengths. However, their inevitable instability and low charge transfer efficiency have prevented their widespread applications. A strategy that can improve both stability and charge separation efficiency is desperately required. Herein, by introducing an *in situ* structural transformation strategy, hydrophobic hierarchically porous $CsPbBr_3$@Pb-MOF is obtained which exhibits high durability in water for more than 7 weeks and appealing thermal stability and resistance to anion intrusion. Meanwhile, abundant oxygen vacancies are detected which efficiently suppress the photogenerated charge recombination. As a result, impressive $CO_2$ photoreduction activity is achieved with $CsPbBr_3$@Pb-MOF as a catalyst. Through a gas–solid reaction (without sacrificial agents and photosensitizers), this $CsPbBr_3$@Pb-MOF-2 composite exhibits a CO yield of 107 μmol $g^{-1}$ $h^{-1}$ with 99.2% selectivity under visible-light ($\lambda$ > 420 nm) irradiation, surpassing most reported $CsPbX_3$-based photocatalysts under similar conditions.

Received 30th March 2023,
Accepted 11th July 2023

DOI: 10.1039/d3qi00596h

rsc.li/frontiers-inorganic



## 1. Introduction

Excessive carbon dioxide ($CO_2$) emissions have greatly affected the balance of the natural carbon cycle, causing a greenhouse effect.[1] The direct conversion of $CO_2$ has been considered as a potential strategy for alleviating both global warming and energy shortages.[2] Lead halide perovskite ($CsPbBr_3$) nanocrystals (NCs) have emerged as an encouraging photocatalyst for various reactions including $CO_2$ reduction,[3–5] pollutant degradation,[6–8] hydrogen production,[9] and organic synthesis[10,11] due to their optimal band structure, high molar extinction coefficient, and long charge-carrier diffusion lengths.[12–14] However, pure $CsPbBr_3$ still faces two major obstacles including the inherent low stability and serious photogenerated electron–hole recombination, which limit its applications in photocatalysis.[15–17] To overcome instability problems, encapsulating pure $CsPbBr_3$ into a protective matrix is considered to be a promising strategy. For example, $SiO_2$,[18,19] zeolites,[20] glass,[21–23] and polymers[24,25] have been used as matrixes for the protection of all-inorganic perovskites. Concerning photogenerated charge recombination, the construction of $CsPbBr_3$-based heterojunctions has been proven to be an efficacious route. Metal oxides,[26–28] g-$C_3N_4$,[29] and graphene[30] have been coupled with $CsPbBr_3$ to reduce charge recombination. However, a strategy that simultaneously improves the stability and charge separation of pure $CsPbBr_3$ is still underexplored.

Recently, metal–organic frameworks (MOFs) have emerged as photocatalysts, photocatalytic hosts, and cocatalysts for $CO_2$ photoreduction, garnering significant attention. This interest stems from their remarkable attributes such as distinctive electronic band structures, exceptional $CO_2$ adsorption capacities, and customizable light-absorption capabilities.[31–33] MOFs have recently been established as promising host matrixes to protect and enhance the physicochemical properties of pure $CsPbBr_3$ NCs because of their tunable porous structure and chemical functionality.[34–36] As we know, the preparation tech-

[a]*School of Materials Science and Engineering, Changchun University of Science and Technology, Changchun, 130022 Jilin, China*
[b]*Jilin Provincial Science and Technology Innovation Center of Optical Materials and Chemistry, School of Chemistry and Environmental Engineering, Changchun University of Science and Technology Changchun, Changchun, 130022 Jilin, China. E-mail: zmsu@nenu.edu.cn*
[c]*Key Laboratory of Polyoxometalate Science of Ministry of Education, Northeast Normal University, Changchun, 130024 Jilin, China. E-mail: suncy009@nenu.edu.cn*
[d]*State Key Laboratory of Supramolecular Structure and Materials, Institute of Theoretical Chemistry, College of Chemistry, Jilin University, Changchun, 130021 Jilin, China*

†Electronic supplementary information (ESI) available. See DOI: https://doi.org/10.1039/d3qi00596h

nique largely determines the structures and performance of perovskite@MOF composites. Normally, the preparation methods of perovskite@MOFs can be broadly classified into four categories: (1) "ship-in-bottle" (ship refers to perovskites, bottle refers to MOFs), (2) "bottle-around-ship", (3) Pb-MOF conversion, and (4) one-pot strategy.[35] The most prevalent "ship-in-bottle" strategy involves introducing precursors of a perovskite (*e.g.*, Pb, Cs, Br, ions) into a prepared beforehand MOF inside which the perovskite can assemble subsequently.[37] To implement this methodology, Lu *et al.*[38] employed pre-synthesized Fe-doped PCN-221 and subjected it to treatment involving a $PbI_2$ solution, resulting in the formation of $PbI_2$@PCN-221($Fe_x$). In the subsequent step, the $PbI_2$@PCN-221($Fe_x$) composite underwent further treatment, this time utilizing an ethanolic solution of $CH_3NH_3I$, leading to the creation of the exquisite hybrid $MAPbI_3$@PCN-221($Fe_x$). However, the diffusion of perovskite precursors into MOFs is largely restricted by the microporous structure of MOFs, which often results in the generation of substantial quantities of perovskites on the surface of MOFs rather than within their pores. Concerning the "bottle-around-ship" strategy, the pre-prepared perovskite is distributed in the precursor solution of the MOF. Subsequently, the assembly of the MOF is initiated to embed the perovskite. For example, Su *et al.*[39] achieved the growth of a zinc/cobalt zeolite imidazole coating on the surface of $CsPbBr_3$ quantum dots (QDs). High temperatures and polar solvents are precisely indispensable in the nucleation and building of MOFs but are harmful to the perovskite structure. In contrast, the "one-pot strategy" of premixing both MOFs and perovskite precursors to produce MOFs and perovskites simultaneously or sequentially is a highly desirable strategy due to the time, energy, and cost savings. To prepare $MAPbBr_3$@ZIF-8, all components required for the synthesis of ZIF-8 ($Zn(NO_3)_2$ and 2-methylimidazole) and $MAPbBr_3$ ($PbBr_2$ and MABr) were mixed and stirred in methanol/DMF solvent at room temperature by Mollick *et al.*[40] However, with the "one-pot strategy", the location and size of the perovskite generated in the MOF cannot be easily manipulated. Recently, through "Pb-MOF conversion", the lead metal nodes of Pb-MOF are picked as the source of Pb for perovskite construction, which facilitates the preparation of composites, minimizes perovskite aggregation, and shortens the electron transportation path.[41–43] Using this approach, Li *et al.*[41] reported the growth of perovskite nanocrystals (NCs) within the confines of the Pb-MOF structure through a direct conversion reaction between halide salt and the Pb-MOF. Nevertheless, the *in situ* growth of a perovskite in Pb-MOF may occupy and destroy the porous structure and affect the applications requiring porosity. Therefore, the development of a strategy that facilitates the introduction of perovskites into MOFs while preserving the porous structure and rendering the composite functionalities remains the central task.

Herein, *via* an *in situ* structural transformation strategy, hydrophobic hierarchically porous $CsPbBr_3$@Pb-MOF with oxygen vacancies is successfully prepared based on a lead bromide-based MOF (PbBr-MOF) and the corresponding cesium bromide salt (CsBr). As expected, the hydrophobic Pb-MOF host significantly increased the stability of pristine $CsPbBr_3$ NCs. More importantly, the oxygen vacancies confined in $CsPbBr_3$@Pb-MOF effectively inhibit the photogenerated electron–hole recombination of $CsPbBr_3$. The produced $CsPbBr_3$@Pb-MOF is used for $CO_2$ photocatalytic reduction through the gas–solid mode without sacrificial agents and photosensitizers. This composite exhibits an exceptional CO yield of 107 μmol $g^{-1}$ $h^{-1}$ with 99.2% selectivity under visible light irradiation ($\lambda$ > 420 nm), representing an improvement of 8.9 times over the yield observed with pure $CsPbBr_3$ (12 μmol $g^{-1}$ $h^{-1}$, 88% selectivity). The possible mechanisms responsible for the photoreduction of $CO_2$ are well studied.

## 2. Experimental

### 2.1 Materials

Lead bromide ($PbBr_2$, 99.9%), lead nitrate ($Pb(NO)_3$, 99%), cesium bromide (CsBr, 99%), terephthalic acid (TPA, >99%), trimesic acid (BTC, $C_6H_3(CO_2H)_3$, 98%), oleic acid (OA, 80%–90%), oleylamine (OM, 90%), triethylamine ($C_6H_{15}N$, 99.0%), toluene ($C_7H_8$, 99%), *N*,*N*-dimethylformamide (DMF, 99.5%), methanol ($CH_3OH$, 99.5%), fuming nitric acid ($HNO_3$, ≥95%), ethanol ($CH_3CH_2OH$, 99.5%), and *n*-hexane ($C_6H_{14}$, >99%) were purchased from Aladdin Co. Ltd.

### 2.2 Synthesis

**2.2.1 Preparation of PbBr-MOF.** The solvothermal approach was used to create PbBr-MOF with a little change to the prior procedure.[44] For the typical synthesis of PbBr-MOF 0.1835 g $PbBr_2$ (0.5 mmol), 0.2640 g terephthalic acid (1.60 mmol), 120 μL nitric acid, ethanol (1.5 mL), and DMF (2.5 mL) were mixed introduced into a 20 mL Teflon reactor, kept at 100 °C for 72 h, and then cool down naturally. Finally, the obtained rod-like crystals were rinsed with DMF and ethanol and dried in a natural environment.

**2.2.2 Solvothermal preparation of $CsPbBr_3$@Pb-MOF.** To prepare $CsPbBr_3$@Pb-MOF, PbBr-MOF (20 mg), CsBr (15, 30, 45 mg), methyl alcohol (4 mL), and deionized water (0.1 mL) were loaded into a 25 mL Teflon reactor, reacted at 190 °C for 2 h, then cooled. The precipitates generated were repeatedly rinsed with $H_2O$. We have labeled the samples with different concentrations of $CsPbBr_3$ as $CsPbBr_3$@Pb-MOF-1, $CsPbBr_3$@Pb-MOF-2, and $CsPbBr_3$@Pb-MOF-3, respectively.

**2.2.3 Preparation of $CsPbBr_3$@Pb-MOF without oxygen vacancy.** $CsPbBr_3$@Pb-MOF without oxygen vacancies was synthesized using a one-pot ultrasonic method. In detail, $Pb(NO)_3$ (0.1 mmol), BTC (0.1 mmol), CsBr (0.1 mmol), and OM (4 mL) were sequentially added to deionized water (8 mL) and subjected to 30 minutes of sonication. The resulting oil phase solution was separated and washed multiple times with *n*-hexane. Afterward, the obtained precipitate was dried at 80 °C for 4 hours. The resulting sample was named $CsPbBr_3$@Pb-MOF-WOV.

**2.2.4 Preparation of Pb-MOF.** To prepare Pb-MOF, PbBr-MOF (20 mg), methyl alcohol (4 mL), and deionized water (0.1 mL) were loaded into a 25 mL Teflon reactor, reacted at 190 °C for 2 h, and then cooled. The precipitates generated were repeatedly rinsed with $H_2O$.

**2.2.5 Preparation of pure $CsPbBr_3$.** $CsPbBr_3$ NCs were synthesized using a process modified from a reported work.[45] At room temperature, $PbBr_2$ (0.2 mmol) and CsBr (0.2 mmol) were dispersed in DMF (8 mL). After complete dissolution, OM (2 mL) and OA (2 mL) were added to the aforementioned solution. To synthesize $CsPbBr_3$ NCs, the precursor was promptly added to toluene (5 mL). The synthesis of $CsPb(BrCl)_3$ and $CsPb(BrI)_3$ was comparable to that of $CsPbBr_3$. The difference in the preparation was that $CsBr_2$ was replaced by $CsCl_2$ or $CsI_2$.

**2.2.6 Synthesis of general Pb-MOF.** General Pb-MOF was synthesized using the procedure of a reported work.[46] The mixture of $Pb(NO)_3$ (0.331 g, 1.0 mmol), terephthalic acid (0.166 g, 1.0 mmol), $H_2O$ (10 mL), and ethanol (2 mL) was placed in a 20 mL Teflon reactor. Then, to achieve a pH of about 4.0 in the solution, triethylamine (0.4 mL) was added. The Teflon reactor was placed in an oven at 160 °C for 4 days and then cooled down to the surrounding ambient temperature. We could obtain the pale-yellow crystals after washing them with $H_2O$ several times.

### 2.3 Photocatalytic $CO_2$ reduction experiments

A solid–gas mode was used to test the $CO_2$ photoreduction performances of the as-prepared samples. Firstly, 10 mg catalysts were dispersed in 1 mL hexane and dropped on a 1 cm × 2 cm glass substrate. Next, to avoid interference with the experimental results, excess organic solvents were removed by vacuum drying. The prepared films and 100 μL water as a reducing agent were put in a 50 mL sealed Pyrex bottle. Before illumination, the reactor atmosphere was replaced with $CO_2$ (99.99%) for 30 min to remove other gases. As the light source, a 300 W Xe lamp (cut-off 420 nm) was employed and the light intensity was maintained at 120 mW $cm^{-2}$. In order to detect CO during the reaction, 0.5 mL of the photocatalyzed mixed gas was fed into a flame ionization detector (FID) for gas chromatography. 1 mL of the gas was injected into a gas chromatography-thermal conductivity detector (GC-TCD) to detect $H_2$. The isotope examination was performed under identical photocatalytic reaction conditions and $^{13}CO$ was determined by GC-MS. Cycling experiments were performed under the same conditions and the samples were directly transferred and reused in the next cycle.

### 2.4 Electrochemical measurements

A CHI760E electrochemical analyzer with a three-electrode setup was used to conduct each photoelectrochemical measurement. As the working electrode, fluorine-doped tin oxide (FTO) glass (1 × 1 $cm^2$) was covered with a photocatalyst. Ag/AgCl (in saturated KCl) and a Pt slice (1 × 1 $cm^2$) were adopted as reference electrodes and counter electrodes, respectively. The 1-butyl-3-methylimidazolium hexafluorophosphate (TBAPF6) $CH_2Cl_2$ solution (0.2 mol) worked as the electrolyte.

### 2.5 Material characterization

Powder X-ray diffraction (PXRD) patterns were performed on a Rigaku Ultima IV using Cu Kα radiation ($\lambda$ = 1.54056 Å). A JEM-2010 was used to capture transmission electron microscopy (TEM) and high-resolution transmission electron microscopy (HRTEM) images. Scanning electron microscopy (SEM) and energy-dispersive X-ray spectroscopy (EDS) were conducted using SU8010. $N_2$ adsorption–desorption isotherms were collected using a MIC-ASAP 2460 instrument at 77 K. Surface wettability was measured using a Phoenix 300. $CO_2$ adsorption isotherms were collected using a MIC-ASAP 2460 instrument at 298 K. X-ray photoelectron spectroscopy (XPS) was conducted on an Escalab 250 instrument. Using a TU-1900 UV-Vis spectrophotometer, UV-Vis diffuse reflectance spectra (UV-vis DRS) were recorded. The emission lifetime was analyzed using a FLS1000 fluorescence spectrometer. The gas product was collected using a GC-9800 gas chromatograph. $^{13}CO_2$ and $H_2{}^{18}O$ isotope experiments were conducted using an HP 6890GC-5973MSD gas chromatography-mass spectrometer. Using a Bruker EMXplus instrument, electron paramagnetic resonance (EPR) signals were acquired. Inductively coupled plasma mass spectrometry (ICP-MS) was tested using an Agilent 7900 instrument.

## 3. Results and discussion

### 3.1 Design and fabrication of $CsPbBr_3$@Pb-MOF

A lead bromide-based MOF (PbBr-MOF) was deliberately selected as the matrix MOF and prepared according to a reported method with adjustments (Fig. S1†).[44] In the structures, zigzag $[Pb_2Br_3]^+$ chains as the secondary building units (SBUs) are coordinated by terephthalic acid (Fig. S2†). $CsPbBr_3$ encapsulated composites were synthesized using PbBr-MOF and CsBr as raw materials under solvothermal conditions (Fig. 1). In comparison with the method used by Lu *et al.*[38] for preparing the composites using the "ship-in-bottle" approach, our method offers a simpler preparation process, while the "ship-in-bottle" approach has advantages in controlling the proportions of each component. Strong emissions were observed under a UV lamp (365 nm) excitation, implying that $CsPbBr_3$ may be formed (Fig. S3†). While keeping the amount of PbBr-MOF constant, we varied the dosage of CsBr (15, 30, and 45 mg) to obtain samples with different concentrations of $CsPbBr_3$ within Pb-MOF, that were respectively denoted as $CsPbBr_3$@Pb-MOF-1, $CsPbBr_3$@Pb-MOF-2, and $CsPbBr_3$@Pb-MOF-3. Furthermore, the content of Cs in the $CsPbBr_3$@Pb-MOF composite materials was determined using inductively coupled plasma mass spectrometry (ICP-MS), yielding values of 0.8% ($CsPbBr_3$@Pb-MOF-1), 2.7% ($CsPbBr_3$@Pb-MOF-2), and 3.3% ($CsPbBr_3$@Pb-MOF-3), respectively.

### 3.2 Characterization of $CsPbBr_3$@Pb-MOF

Initially, the crystal structures of $CsPbBr_3$, Pb-MOF, and $CsPbBr_3$@Pb-MOF composites were investigated using powder X-ray diffraction (PXRD) analysis (Fig. 2a and Fig. S4†). For

 

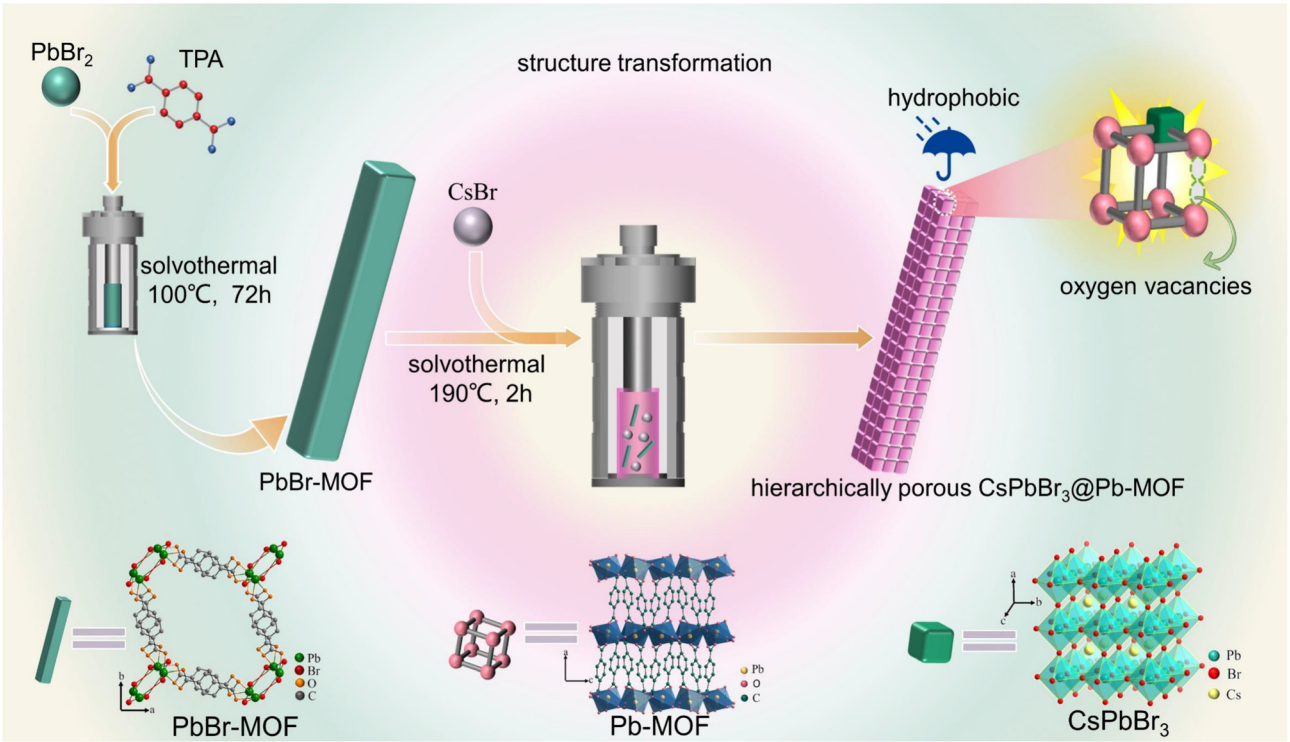


**Fig. 1** A schematic diagram for the synthesis of $CsPbBr_3$@Pb-MOF.

sample $CsPbBr_3$@Pb-MOF-1, no characteristic peaks corresponding to $CsPbBr_3$ were observed, due to its low concentration. For both $CsPbBr_3$@Pb-MOF-2 and $CsPbBr_3$@Pb-MOF-3, the successful combination of $CsPbBr_3$ NCs was indicated by powder X-ray diffraction (PXRD), in which three distinctive peaks at 21.4, 26.3, and 43.5° corresponded to the (110), (111), and (220) planes of cubic $CsPbBr_3$ (PDF#75-0412), respectively.[47] A notable observation was the significantly stronger intensity of the characteristic peaks of $CsPbBr_3$ in $CsPbBr_3$@Pb-MOF-3 compared to $CsPbBr_3$@Pb-MOF-2, attributed to the higher content of $CsPbBr_3$ in $CsPbBr_3$@Pb-MOF-3 compared to $CsPbBr_3$@Pb-MOF-2. However, to our surprise, the characteristic diffraction peaks belonging to the PbBr-MOF matrix almost disappeared and are replaced by a new set of diffraction peaks. In order to clarify this issue, the parent MOF was subjected to solvothermal conditions. The obtained powder samples were tested by PXRD and it was found that their diffraction peaks basically corresponded to the diffraction peaks in the perovskite composites, suggesting that the structure of PbBr-MOF was transformed under solvothermal synthesis (Fig. S5 and S6†).[44,46] The elements and their contents in the transformed materials were examined by energy-dispersive X-ray (EDX). In EDX, Pb, C, and O were detected in equal distribution, suggesting that Br ions of PbBr-MOF are shed during the structural transformation (Fig. S7†). Combined with the PXRD results, we boldly speculate that PbBr-MOF is likely to be transformed into Pb-MOF. To confirm the structural stability, we study the PXRD pattern of PbBr-MOF and Pb-MOF after water immersion (Fig. S8†). The major peaks of PbBr-MOF disappeared after being immersed for 10 min in water, while the peaks of Pb-MOF remained intact, suggesting that Pb-MOF is extremely stable in water. During the test, we found that powdery Pb-MOF can float on the surface of the water. We speculate that the excellent water stability may result from its hydrophobicity. The water contact angle of 140° verifies this prediction (Fig. S9†).[48] Pb-MOF with a hydrophobic interface makes it a promising candidate for the protection of $CsPbBr_3$. For comparison, we tried to synthesize this MOF using $Pb(NO)_3$ and terephthalic acid as the precursor. Fortunately, crystals of this MOF (denoted as general Pb-MOF, see more details in Experimental sections) were obtained and its structure was resolved in which Pb ions are octahedrally coordinated by terephthalic acid. By comparing its PXRD patterns, we could find that they matched each other very well, indicating that the transformed structure is Pb-MOF (Fig. S10†). The generated composite was therefore named $CsPbBr_3$@Pb-MOF. We speculate that the solvothermally induced *in situ* structural transformation provides a prerequisite for the growth of the perovskite in $CsPbBr_3$@Pb-MOF. The broken Pb–Br bond releases occupied Pb sites, which are crucial for the formation of the $CsPbBr_3$ perovskite, meanwhile, the detached halogen is also considered an important component of the perovskite.

The structure of the composite was further understood by transmission electron microscopy (TEM), high-resolution transmission electron microscopy (HRTEM), energy dispersive

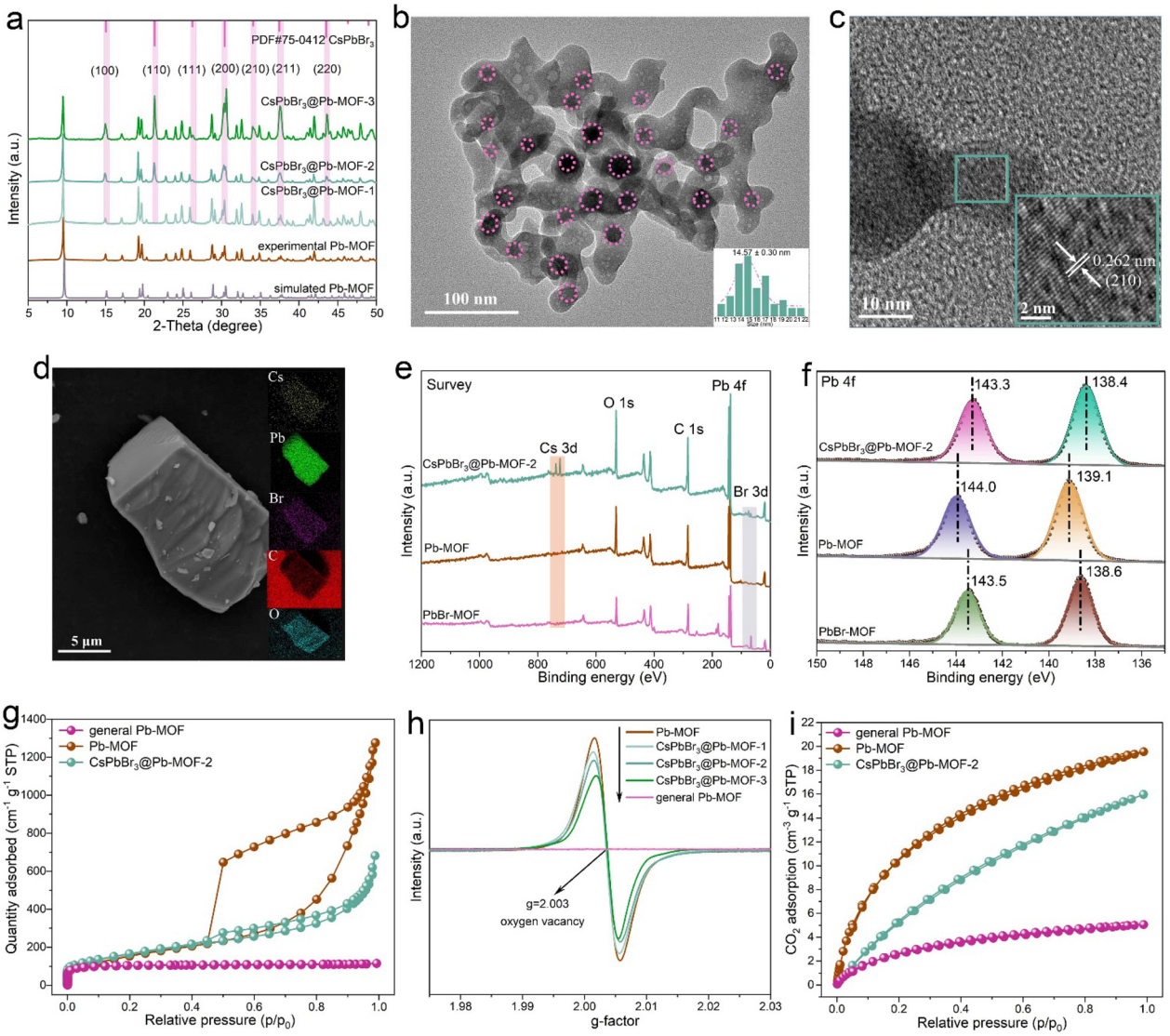


**Fig. 2** (a) PXRD patterns of $CsPbBr_3$@Pb-MOF. (b) TEM image of $CsPbBr_3$@Pb-MOF-2, dark dots in the figure are $CsPbBr_3$ NCs. Inset of (b) shows particle size distributions of $CsPbBr_3$ NCs. (c) The HRTEM image of $CsPbBr_3$@Pb-MOF. Inset of (c) shows the lattice fringe of $CsPbBr_3$ NCs. (d) SEM image and EDX mapping of $CsPbBr_3$@Pb-MOF-2. XPS analysis of the samples: (e) survey spectra and (f) Pb 4f spectra. (g) $N_2$ adsorption–desorption isotherms of general Pb-MOF, Pb-MOF, and $CsPbBr_3$@Pb-MOF-2 at 77 K. (h) Electron paramagnetic resonance spectra of general Pb-MOF, Pb-MOF, and $CsPbBr_3$@Pb-MOF. (i) $CO_2$ adsorption–desorption isotherms of general Pb-MOF, Pb-MOF, and $CsPbBr_3$@Pb-MOF-2 at 298 K.

X-ray (EDX) spectroscopy, X-ray photoelectron spectroscopy (XPS), electron paramagnetic resonance (EPR) and gas adsorption. TEM and HRTEM measurements were performed and depicted in Fig. 2b and c. In Fig. 2b, we can see that the $CsPbBr_3$ NCs marked with circles, indicating a size of 14.75 ± 0.30 nm, are uniformly embedded in the Pb-MOF host without significant aggregations. As shown in Fig. S11,† pure $CsPbBr_3$ NCs exhibit uniform cubic shapes with an average particle size of 10.24 ± 0.07 nm. As illustrated in Fig. 2c, HRTEM images show lattice spaces of 0.262 nm, which are a good match with the (210) plane of cubic $CsPbBr_3$.[49] In Fig. 2d, the EDX mapping of $CsPbBr_3$@Pb-MOF-2 indicates that Cs, Pb, Br, C, and O are uniformly distributed in the matrix. XPS measurements are shown in Fig. 2e and f. In the comparison between PbBr-MOF and Pb-MOF, the Br 3d signal belonging to PbBr-MOF is not seen for Pb-MOF. In addition, when compared with Pb-MOF, signals for new Br and Cs species are observed in $CsPbBr_3$@Pb-MOF-2 composites. For a more detailed analysis, high-resolution XPS spectra of Pb 4f are presented in Fig. 2f. For PbBr-MOF, Pb 4f spectra show two prominent peaks at 143.5 ($4f_{5/2}$) and 138.6 eV ($4f_{7/2}$).[50] In addition, the Pb $4f_{5/2}$ and Pb $4f_{7/2}$ peaks of Pb-MOF were shifted to 144.0 and 139.1 eV, respectively, due to the change in the coordination environment of the Pb atom during the structural transformation (the breaking of Pb–Br bonds and reorganization of Pb with carboxylic acid ligands). Of note, in comparison with Pb-MOF, the Pb 4f bands of $CsPbBr_3$@Pb-MOF-2 demonstrates a 0.7 eV shift to the lower binding energy after the growth of

 

$CsPbBr_3$ in Pb-MOF. This phenomenon indicates that the Pb node in Pb-MOF is coordinated with Br to produce a new Pb–Br bond belonging to $CsPbBr_3$.[41,51]

$N_2$ adsorption–desorption isotherms of general Pb-MOF, Pb-MOF, and $CsPbBr_3$@Pb-MOF-2 were collected at 77 K to evaluate porosity and the specific surface area, as illustrated in Fig. 2g. The curves for general Pb-MOF are a type I isotherm, signifying the presence of microporosity.[52] Moreover, the $N_2$ adsorption–desorption isotherms of Pb-MOF reveal a combination mode of type I and type IV, implying the simultaneous existence of micropores and mesopores.[52,53] On the other hand, intrinsic micropores (<2 nm) are maintained, while mesoporous features (concentrated at 4 nm) appear in Pb-MOF in the pore size distribution curve (Fig. S12†). The Brunauer–Emmett–Teller (BET) surface area of Pb-MOF is determined to be 904.58 $m^2\ g^{-1}$, which is bigger than the general Pb-MOF (398.43 $m^2\ g^{-1}$). The rich mesoporous and larger surface area of Pb-MOF are expected to favor mass transport and enhance the utilization of active sites.[47,54] In Fig. 2g, a combination mode of type I and type IV of the $N_2$ adsorption–desorption isotherm is observed for $CsPbBr_3$@Pb-MOF-2.[52] The result confirms the presence of micropores and mesopores in $CsPbBr_3$@Pb-MOF-2.[52,53] Likewise, the pore size distributions of $CsPbBr_3$@Pb-MOF-2 agree with this conclusion (Fig. S13†). Meanwhile, compared with Pb-MOF (904.58 $m^2\ g^{-1}$), $CsPbBr_3$@Pb-MOF (587.68 $m^2\ g^{-1}$) shows lower BET surface areas. Furthermore, apparent mesopores were observed in Pb-MOF on comparing the TEM of general Pb-MOF (Fig. S14†). The generation of mesopores may be ascribed to the *in situ* structural transformation of MOFs which leads to the missing linker defects (Fig. S15†).[53,55,56]

Subsequently, electron paramagnetic resonance (EPR) was used to detect oxygen vacancy, as shown in Fig. 2h. Compared with general Pb-MOF, a symmetrical signal of the oxygen vacancy ($g$ = 2.003) is exhibited in the EPR spectra of Pb-MOF.[57] These results unambiguously suggest the existence of oxygen vacancies in Pb-MOF together with coordinatively unsaturated Pb atoms. Obviously, the symmetric signal belonging to the oxygen vacancy is also revealed in the $CsPbBr_3$@Pb-MOF composite.[57] However, as the content of $CsPbBr_3$ increased in Pb-MOF, a downward trend was observed in the intensity of oxygen vacancies. Such oxygen vacancies can act as electron capture traps that can facilitate photogenerated charge separation.[58] $CO_2$ adsorption is a prerequisite for photocatalytic $CO_2$ reduction. $CO_2$ capture capacities of general Pb-MOF, Pb-MOF, and $CsPbBr_3$@Pb-MOF-2 were evaluated from $CO_2$ adsorption isotherms at 297 K, shown in Fig. 2i. The general Pb-MOF and Pb-MOF display $CO_2$ uptakes of 5 and 19.5 $cm^3\ g^{-1}$, respectively. We ascribed the enhanced $CO_2$ adsorption to a higher specific surface area and mesoporous channel in Pb-MOF.[59,60] Correspondingly, the $CO_2$ adsorption amount of $CsPbBr_3$@Pb-MOF-2 (15.9 $cm^2\ g^{-1}$) is between general Pb-MOF and Pb-MOF. The good water stability, abundant oxygen vacancy, mesoporous structure, and higher specific surface area make Pb-MOF a promising host to assist $CsPbBr_3$ for photocatalytic $CO_2$ reduction.[48,54,61]

### 3.3 Optical properties

Along with the structural characteristics mentioned above, the optical characteristics of $CsPbBr_3$@Pb-MOF-2 composites, pure $CsPbBr_3$ NCs and Pb-MOF were also studied, as illustrated in Fig. 3. As shown in Fig. 3a, with ultraviolet-visible (UV-Vis) diffuse reflectance spectroscopy (DRS) the light absorption properties of pure $CsPbBr_3$, Pb-MOF and $CsPbBr_3$@Pb-MOF-2 composites were evaluated. The absorption band edges of Pb-MOF (425 nm), pure $CsPbBr_3$ (520 nm) and $CsPbBr_3$@Pb-MOF-2 (543 nm) samples are in the visible range. However, on coupling $CsPbBr_3$ with Pb-MOF, the absorption edge of $CsPbBr_3$@Pb-MOF-2 was markedly red-shifted, resulting in an apparent enhancement of the sample's light-absorbing capacity. This is of significant importance for the utilization of photocatalysts in a practical setting. The band gap of the samples was calculated using the Kubelka–Munk function,[28] as depicted in Fig. 3b. These calculated values are consistent with previous literature results.[14,20] Based on the reaction thermodynamics, the energy band structure is also critical in photocatalytic performance. Herein, Mott–Schottky (MS) analyses of $CsPbBr_3$ and Pb-MOF were performed and depicted in Fig. 3c and d. Firstly, as shown in Fig. 3b, the bandgaps ($E_g$s) of $CsPbBr_3$ and Pb-MOF were evaluated to be 2.42 eV and 3.08 eV, respectively. In the MS curve, the slope of $CsPbBr_3$ and Pb-MOF demonstrates a positive value, suggesting the samples are n-type characteristic photocatalysts. As known, the MS curve is assessed as a flat band potential and the flat band potential of an n-type semiconductor is 0.1 V lower than its valence band ($E_{CB}$).[62] According to the MS curve, the flat band potential of $CsPbBr_3$ is about −1.10 V *vs.* Ag/AgCl (≈−0.90 V *vs.* NHE) (flat band potential of Pb-MOF is about −0.17 V *vs.* NHE). Therefore, the $E_{CB}$ of $CsPbBr_3$ is −1.00 V *vs.* NHE ($E_{CB}$ of Pb-MOF is −0.27 V *vs.* NHE) and the valence band ($E_{VB}$) of $CsPbBr_3$ was calculated as 1.42 V *vs.* NHE ($E_{VB}$ of Pb-MOF is 2.81 V *vs.* NHE), based on the formula of $E_{CB} = E_{VB} - E_g$. Analyzing the energy level, as illustrated in Fig. 3e, the $E_{CB}$ of $CsPbBr_3$ (−1.00 V *vs.* NHE) is more negative than $CO_2$/CO (−0.52 V *vs.* NHE) and $O_2/{}^{\bullet}O_2^-$ (−0.33 V *vs.* NHE) and the $E_{VB}$ of $CsPbBr_3$ (0.85 V *vs.* NHE) is more positive than $H_2O/O_2$ (0.81 V).[12] As for Pb-MOF, the $E_{CB}$ of Pb-MOF (−0.27 V *vs.* NHE) is not more negative than $CO_2$/CO (−0.52 V *vs.* NHE) and $O_2/{}^{\bullet}O_2^-$ (−0.33 V *vs.* NHE). But the $E_{VB}$ of Pb-MOF (2.81 V *vs.* NHE) is more positive than $H_2O/O_2$ (0.81 V), $H_2O/{}^{\bullet}OH$ (1.99 V) and $OH^-/{}^{\bullet}OH$ (2.34 V). To further verify the energy band structure of $CsPbBr_3$@Pb-MOF-2, $CsPbBr_3$ and Pb-MOF, electron paramagnetic resonance (EPR) analysis was executed. For EPR studies, the sample was dissolved in 5,5-dimethyl-1-pyrroline *N*-oxide (DMPO, capture agent of the spin electron) to identify ${}^{\bullet}O_2^-$ and ${}^{\bullet}OH$, respectively.[26,63] In Fig. 3f, it can be seen that under visible-light irradiation conditions, Pb-MOF did not exhibit the characteristic peaks of DMPO-${}^{\bullet}O_2^-$. In comparison, the characteristic signals of DMPO-${}^{\bullet}O_2^-$ are successfully detected in $CsPbBr_3$@Pb-MOF-2 and $CsPbBr_3$ NCs. In addition, the peak intensity of $CsPbBr_3$@Pb-MOF-2 is much stronger than

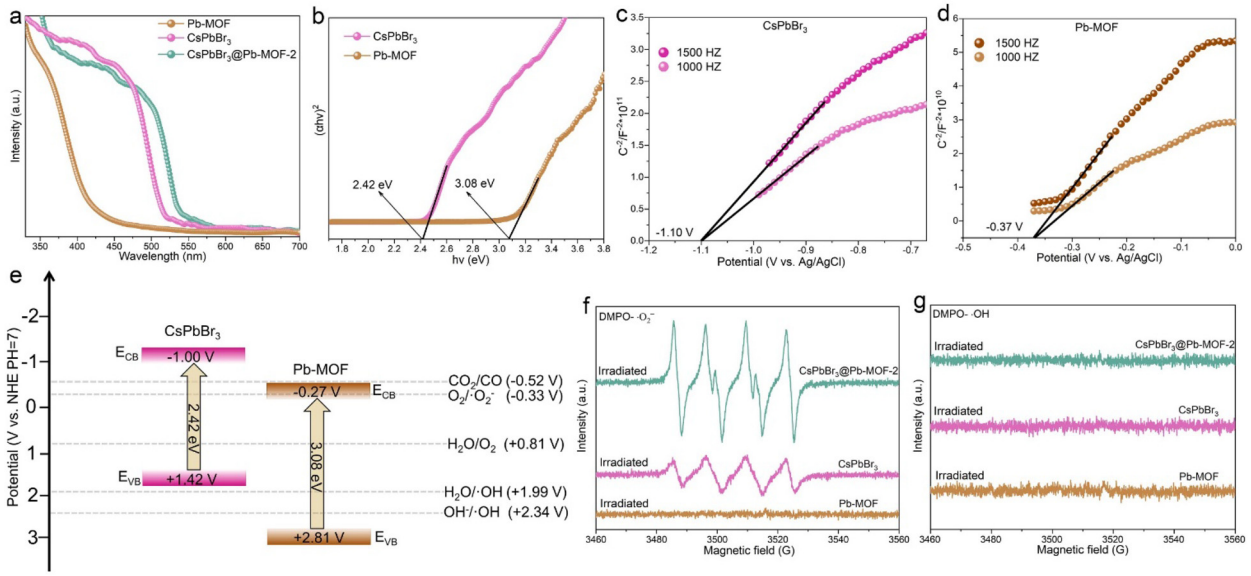


**Fig. 3** (a) UV-vis diffuse reflectance spectra of Pb-MOF, $CsPbBr_3$ and $CsPbBr_3$@Pb-MOF-2. (b) The band gap spectra of $CsPbBr_3$ and Pb-MOF. Mott–Schottky plots of (c) $CsPbBr_3$ and (d) Pb-MOF. (e) Schematic illustration of the potential energy diagram for $CsPbBr_3$ and Pb-MOF. Electron paramagnetic resonance spectra of (f) DMPO-$^{\bullet}O_2^-$ and (g) DMPO-$^{\bullet}$OH in the presence of $CsPbBr_3$@Pb-MOF-2, $CsPbBr_3$ and Pb-MOF.

$CsPbBr_3$ NCs, suggesting $CsPbBr_3$@Pb-MOF-2 possesses a higher electron transfer efficiency. As shown in Fig. 3g, on irradiating Pb-MOF, $CsPbBr_3$ NCs and $CsPbBr_3$@Pb-MOF-2, no typical peak of DMPO-$^{\bullet}$OH is detected, indicating the possible formation of a Z-scheme heterojunction between $CsPbBr_3$ and Pb-MOF.[64] This observation highlights the essential role of oxygen vacancies in Pb-MOF in facilitating the transfer of photogenerated electrons between $CsPbBr_3$ and Pb-MOF. Meanwhile, the band positions of $CsPbBr_3$@Pb-MOF and $CsPbBr_3$ satisfy the thermodynamic requirements for reduction and oxidation reactions, indicating it might be an appropriate catalyst for $CO_2$ reduction.

### 3.4 Water stability, thermal stability, and preventing anion intrusion studies

To check the potential of $CsPbBr_3$@Pb-MOF for photocatalytic applications, we systematically investigated the stability of $CsPbBr_3$@Pb-MOF-2 including water stability, thermal stability, and preventing anion intrusion (Fig. 4). Being ionic crystals, $CsPbBr_3$ NCs readily dissolve in the presence of water, which quenches their luminescence. The PL intensities of $CsPbBr_3$@Pb-MOF-2 remained consistent, displaying approximately 82.6% of their initial strength even after 49 days of immersion in water, as depicted in Fig. 4a (left side) and Fig. S16.† In sharp contrast, when 1 ml of water was added to pure $CsPbBr_3$ NCs dispersed in hexane for 20 min, the fluorescence value of the $CsPbBr_3$ sample was only 1% of the initial value (Fig. 4a, right side). This is attributed to the excellent hydrophobicity exhibited by $CsPbBr_3$@Pb-MOF-2 (water contact angle 140.2°), (Fig. S17†). Next, the thermal stability of $CsPbBr_3$@Pb-MOF-2 was investigated during heating–cooling in the range of 20–120 °C (Fig. 3b). After heating at 120 °C for

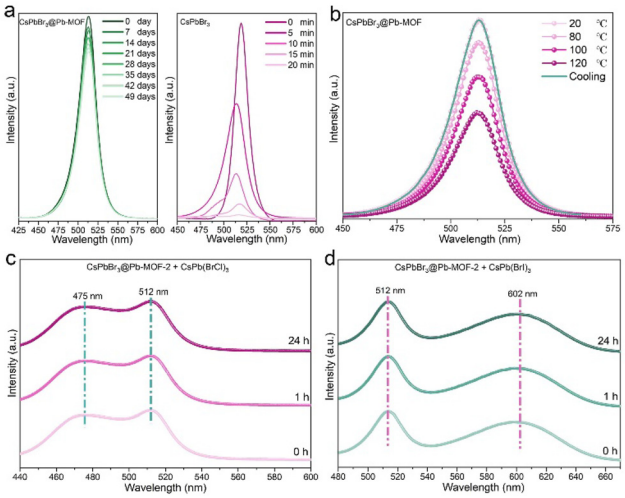


**Fig. 4** (a) PL intensity changes of $CsPbBr_3$@Pb-MOF-2 and $CsPbBr_3$ with time. (b) The PL spectra of $CsPbBr_3$@Pb-MOF-2 as a function of temperature. PL spectra of (c) $CsPbBr_3$@Pb-MOF-2 and $CsPb(BrCl)_3$ and (d) $CsPbBr_3$@Pb-MOF-2 and $CsPb(BrI)_3$ mixed powders at different time intervals.

30 min, $CsPbBr_3$@Pb-MOF-2 could retain about 52% of its original PL intensity. Impressively, the PL emission value progressively recovered after cooling (green line), eventually reaching the original value. PXRD of $CsPbBr_3$@Pb-MOF-2 after immersion in water and after heating remains intact further proving their high stability (Fig. S18†). The anion intrusion issue of $CsPbBr_3$ is another shortcoming in the application.[65] To illustrate the behavior of $CsPbBr_3$@Pb-MOF-2, samples containing single and two halogens including $CsPbBr_3$@Pb-MOF-2 and $CsPb(BrCl)_3$, and $CsPbBr_3$@Pb-MOF-2 and CsPb

 

$(BrI)_3$, were mixed and subjected to the environment. As shown in Fig. 4c and d, the position and intensity of the fluorescence peaks of the samples did not change after 24 hours. The excellent water stability, thermal stability, and prevention of anion exchange of this $CsPbBr_3$@Pb-MOF-2 composite can be attributed to the hydrophobic Pb-MOF walls that protect $CsPbBr_3$ from various chemical conditions.[66]

### 3.5 Photoinduced charge separation and transfer dynamics

As known, the photogenerated charge transfer and separation efficiency of the sample have a crucial effect on the photocatalytic efficiency.[12–17] On account of this point, photoelectrochemical, electrochemical, and photoluminescence experiments were performed, as presented in Fig. 5. Firstly, the photocurrent response of $CsPbBr_3$@Pb-MOF-2 and pure $CsPbBr_3$ NCs were measured under turn-on–off cycles of visible-light ($\lambda$ > 420 nm) irradiation. As demonstrated in Fig. 5a, the $CsPbBr_3$@Pb-MOF-2 sample exhibits a significantly higher photocurrent density compared to $CsPbBr_3$ NCs. This result indicates that $CsPbBr_3$@Pb-MOF-2 has a more efficient transfer of photogenerated charge. In other words, oxygen vacancies in Pb-MOF act as a reservoir to receive the photogenerated charge generated by $CsPbBr_3$. Furthermore, the charge transport behaviors of $CsPbBr_3$@Pb-MOF-2 and $CsPbBr_3$ were probed using electrochemical impedance spectroscopy (EIS), as depicted in Fig. 5b. In the Nyquist plot, $CsPbBr_3$@Pb-MOF-2 exhibits smaller semicircle radii owing to small charge transfer resistance.[27] In comparison, pure $CsPbBr_3$ NCs show a larger charge transfer resistance, demonstrating the superb carrier mobility between $CsPbBr_3$ NCs and Pb-MOF. Furthermore, the charge transfer dynamics of $CsPbBr_3$@Pb-MOF and $CsPbBr_3$ NCs are evaluated by steady-state photoluminescence (PL). The fluorescence intensity of $CsPbBr_3$@Pb-MOF-2 was dramatically quenched compared to $CsPbBr_3$ NCs (Fig. 5c), verifying that the recombination of photogenerated charges of $CsPbBr_3$@Pb-MOF-2 was effectively inhibited. Furthermore, the time-resolved PL spectra of $CsPbBr_3$@Pb-MOF-2 and $CsPbBr_3$ NCs were recorded (Fig. 5d). The average lifetime of the samples was observed to decline significantly, from 66.8 ns for pure $CsPbBr_3$ NCs to 12.3 ns for $CsPbBr_3$@Pb-MOF (Table S1†).[30,39] From all the above experiments, we believe that the enhanced photogenerated charge separation in $CsPbBr_3$@Pb-MOF-2 may be due to the introduced oxygen vacancies acting as charge capture centers.

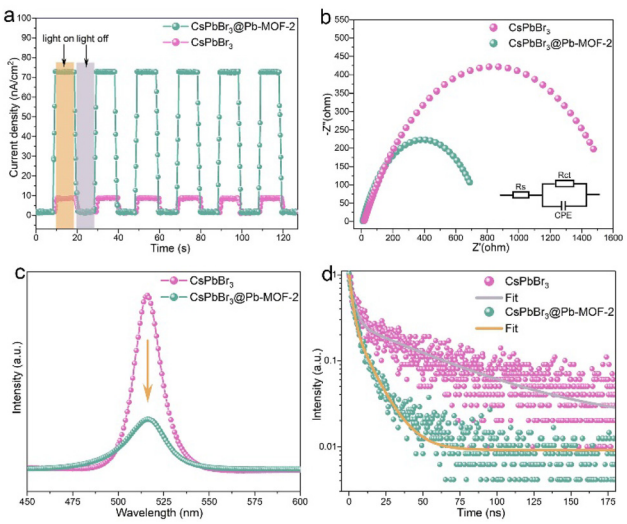


**Fig. 5** (a) Photocurrent responses of the samples at −0.4 V *vs.* Ag/AgCl under visible light irradiation ($\lambda$ > 420 nm). (b) Electrochemical impendence spectra of the samples. The inset of (b) shows the equivalent circuit diagram, $R_s$: solution resistance, $R_{ct}$: interface charge transfer resistance, CPE: constant phase element. (c) Steady-state PL spectra with a 365 nm excitation wavelength. (d) Time-resolved PL decay plots with a 365 nm excitation wavelength and a 516 nm emission wavelength.

### 3.6 Photocatalyst activity tests

This as-synthesized $CsPbBr_3$@Pb-MOF, $CsPbBr_3$@Pb-MOF-WOV (Fig. S19†), pure $CsPbBr_3$ NCs, and pure Pb-MOF were further explored by $CO_2$ photoreduction in the gas–solid mode with $H_2O$ as the reductant, without using any sacrificial reagent or photosensitizers (Fig. S20†). Under visible-light ($\lambda$ > 420 nm) irradiation, for $CsPbBr_3$@Pb-MOF, $CsPbBr_3$@Pb-MOF-WOV and $CsPbBr_3$ NCs, CO is the main reduction product along with a trace of $H_2$. $CsPbBr_3$@Pb-MOF exhibits ≥99.2% selectivity towards CO production, while pure $CsPbBr_3$ NCs and $CsPbBr_3$@Pb-MOF-WOV only show 88% and 90.0 selectivities (Table S2†). The high selectivity of $CsPbBr_3$@Pb-MOF may be attributed to its hydrophobic surface depressing $H_2$ production (Fig. S21†).[67] In Fig. 6a, $CsPbBr_3$@Pb-MOF-2 displays the highest CO production rate of 107 μmol $g^{-1}$ $h^{-1}$, which is 8.9 times higher than that of pure $CsPbBr_3$ NCs (12 μmol $g^{-1}$ $h^{-1}$). Simultaneously, the CO production of $CsPbBr_3$@Pb-MOF-2 was about 3.7 and 1.2 times higher than that of $CsPbBr_3$@Pb-MOF-1 (29 μmol $g^{-1}$ $h^{-1}$) and $CsPbBr_3$@Pb-MOF-3 (89 μmol $g^{-1}$ $h^{-1}$),

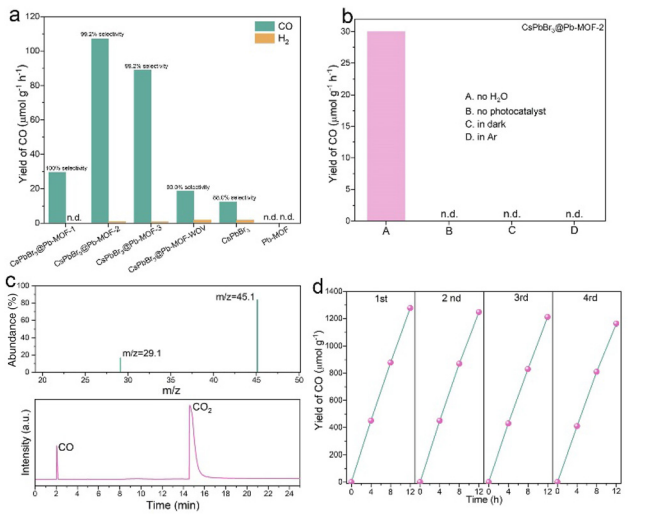


**Fig. 6** (a) Photoreduction $CO_2$ performances of the samples. (b) The photocatalytic performance of $CsPbBr_3$@Pb-MOF-2 under different conditions. (c) The GC chromatogram and GC-mass result of an isotopic experiment using $^{13}CO_2$. (d) 48 h recycle photocatalytic $CO_2$ reduction using $CsPbBr_3$@Pb-MOF-2.

indicating that an appropriate concentration of oxygen vacancies and perovskite content can optimize CO yield. In contrast, the CO production of $CsPbBr_3$@Pb-MOF-WOV was only 18 μmol $g^{-1}$ $h^{-1}$, highlighting the crucial role of oxygen vacancies in enhancing the CO yield. As for Pb-MOF, no CO or $H_2$ could be observed. The CO yield of $CsPbBr_3$@Pb-MOF-2 is also comparable to the reported highest perovskite-based photocatalysts in gas–solid phase and liquid–solid phase photocatalysis (Table S3†). To confirm the actual roles of each component during the photocatalytic reduction of $CO_2$, control experiments were conducted, as shown in Fig. 6b. When $H_2O$ was removed from the system, the CO yield decreased to 30 μmol $g^{-1}$ $h^{-1}$, indicating a significant contribution of $H_2O$ as the electron/proton source. The absence of light and photocatalyst resulted in no detection of CO, affirming the crucial role of both light and photocatalyst in the photoreduction of $CO_2$. When replacing $CO_2$ with Ar, no CO was observed, indicating CO did not originate from the organic matter in the MOF. To demonstrate this perspective, isotope labeling tests were carried out (Fig. 6c). On replacing $CO_2$ with $^{13}CO_2$ ($m/z$ = 45) as the feedstock, an obvious peak of $^{13}CO$ ($m/z$ = 29) was detected. Therefore, CO was confirmed to be obtained from the photoreduction of $CO_2$. Moreover, the photocatalytic reaction was also investigated using $H_2{}^{18}O$ as a replacement for $H_2O$, and the MS results are shown in Fig. S22.† The corresponding signals at $m/z$ = 28 and $m/z$ = 30 were observed, indicating the formation of $C^{16}O$ and $C^{18}O$, respectively. These findings suggest that the O atom in the produced CO is not solely derived from $CO_2$, but can also originate from $H_2O$. This observation is consistent with the findings reported by Zhang *et al.*[68] Based on the experimental results and the findings of Zhang *et al.*, two possible pathways (Fig. S23 and S24†) for photocatalytic $CO_2$ reduction to produce CO can be presented as follows.

$$CO_2 + 2e^- + 2H^+ \rightarrow CO + H_2O$$

$$H_2O + CO_2 + 2e^- + 2H^+ \rightarrow CO + 2H_2O$$

Given the significance of the stability in the practical application of photocatalysts, a cycling test was performed on $CsPbBr_3$@Pb-MOF-2. As shown in Fig. 6d, only a 9% loss of photocatalytic activity is incurred after 48 h of recycling of the reaction. Moreover, after a 48 h stability test, $CsPbBr_3$@Pb-MOF-2 was subjected to characterization through PXRD, XPS, TEM, and UV-Vis (Fig. S25 and S28†). The results demonstrate the exceptional stability of $CsPbBr_3$@Pb-MOF-2.

### 3.7 The possible photocatalytic mechanism

A possible mechanism for $CO_2$ photoreduction over $CsPbBr_3$@Pb-MOF is proposed based on the above results and analyses, as described in Fig. 7. Firstly, the opportune specific surface area and mesoporous structure of Pb-MOF can benefit from the adsorption and concentration of $CO_2$ and supply abundant active sites, thereby promoting the subsequent photoreduction reaction. Secondly, under light irradiation, $CsPbBr_3$ was excited and released photogenerated electrons ($e^-$) and photogenerated holes ($h^+$). Later, the oxygen vacancies in the Pb-MOF function act as a photogenerated electron acceptor from $CsPbBr_3$. The improved charge transfer between

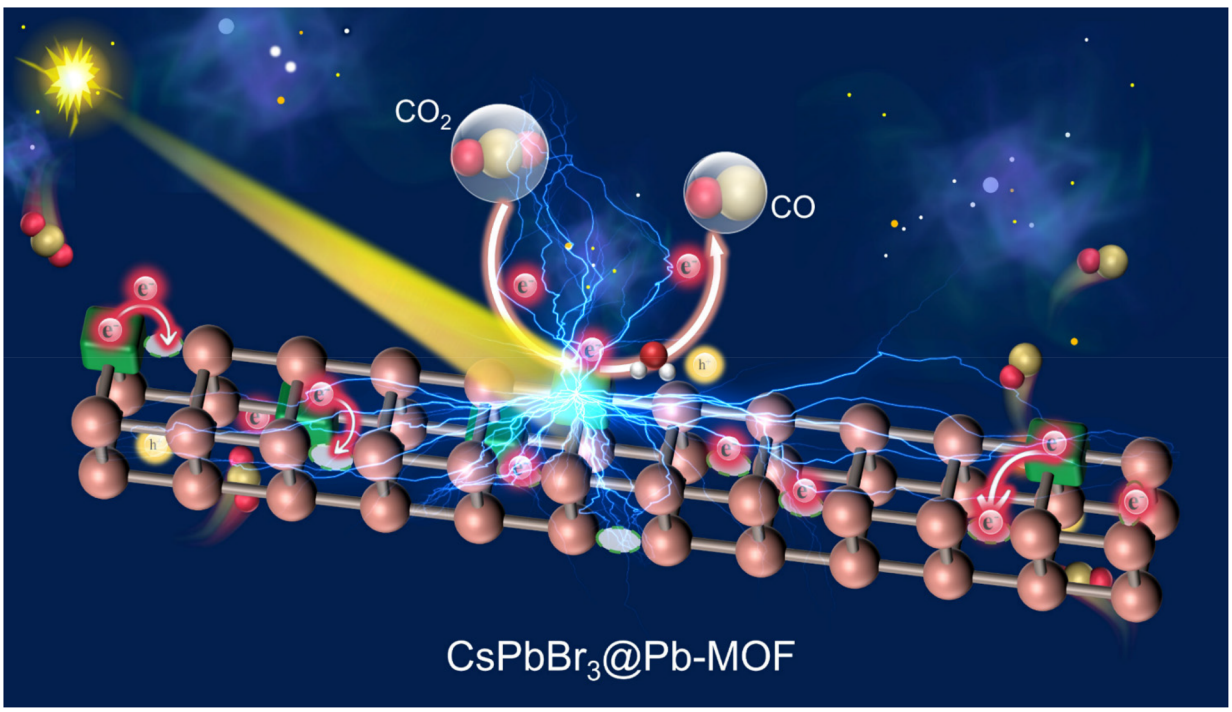


Fig. 7 The possible mechanism of $CO_2$ photoreduction for $CsPbBr_3$@Pb-MOF.

 

$CsPbBr_3$ and Pb-MOF inhibits the radiative recombination of the photogenerated electrons and holes. Thirdly, the enriched electrons on the surface of Pb-MOF undergo a 2-electron reaction to reduce $CO_2$ to CO. Meanwhile, a Pb-MOF hydrophobic surface environment with a high concentration of $CO_2$ boosts the selectivity for $CO_2$ photoreduction, suppressing the generation of the $H_2$ byproduct. Finally, the performance of $CsPbBr_3$ NCs is improved, owing to the synergistic effect of Pb-MOF.

## 4. Conclusions

In summary, we developed a facile and low-cost *in situ* structural transformation strategy to introduce both $CsPbBr_3$ and oxygen vacancies into hydrophobic hierarchically porous Pb-MOF by reacting PbBr-MOF with CsBr. During the structural transformation from PbBr-MOF to Pb-MOF, the exposure of Pb metal nodes in Pb-MOF is involved in the construction of $CsPbBr_3$, which facilitates $CsPbBr_3$@Pb-MOF preparation, minimizes $CsPbBr_3$ aggregation, and shortens the photogenerated electron transportation path. Meanwhile, the organic linker omission in structural transformation results in a hierarchically porous structure and abundant oxygen vacancies which enables fast mass transport and accelerates the photogenerated charge separation. The enhanced stability and outstanding electron transfer efficiency permit $CsPbBr_3$@Pb-MOF-2 to exhibit a significantly impressive photocatalytic performance for $CO_2$ reduction to CO (107 μmol $g^{-1}$ $h^{-1}$, 99.2% selectivity) which is an 8.9-fold improvement over that of pure $CsPbBr_3$ (12 μmol $g^{-1}$ $h^{-1}$, 88% selectivity) under visible-light ($\lambda$ > 420 nm). Our research provides new insights and offers novel perspectives for the development of efficient lead-based perovskite MOF composite photocatalysts.

## Author contributions

The manuscript was written through the contributions of all authors.

## Conflicts of interest

There are no conflicts of interest to declare.

## Acknowledgements

This work was financially supported by the NSFC of China (no. 22271023 and 21971032), the Education Department of Jilin Province (no. JJKH20221153KJ) and Jilin Provincial Department of Science and Technology (no. 20230508108RC).

## References

1 O. S. Bushuyev, P. De Luna, C. T. Dinh, L. Tao, G. Saur, J. van de Lagemaat, S. O. Kelley and E. H. Sargent, What should we make with $CO_2$ and how can we make it?, *Joule*, 2018, **2**, 825–832.
2 Z. Zhang, Y. Zheng, L. Qian, D. Luo, H. Dou, G. Wen, A. Yu and Z. Chen, Emerging trends in sustainable $CO_2$-management materials, *Adv. Mater.*, 2022, **34**, 2201547.
3 Y.-F. Xu, M.-Z. Yang, B.-X. Chen, X.-D. Wang, H.-Y. Chen, D.-B. Kuang and C.-Y. Su, A $CsPbBr_3$ perovskite quantum dot/graphene oxide composite for photocatalytic $CO_2$ reduction, *J. Am. Chem. Soc.*, 2017, **139**, 5660–5663.
4 J. Hou, S. Cao, Y. Wu, Z. Gao, F. Liang, Y. Sun, Z. Lin and L. Sun, Inorganic colloidal perovskite quantum dots for robust solar $CO_2$ reduction, *Chem. – Eur. J.*, 2017, **23**, 9481–9485.
5 S.-H. Guo, J. Zhou, X. Zhao, C.-Y. Sun, S.-Q. You, X.-L. Wang and Z.-M. Su, Enhanced $CO_2$ photoreduction via tuning halides in perovskites, *J. Catal.*, 2019, **369**, 201–208.
6 G. Gao, Q. Xi, H. Zhou, Y. Zhao, C. Wu, L. Wang, P. Guo and J. Xu, Novel inorganic perovskite quantum dots for photocatalysis, *Nanoscale*, 2017, **9**, 12032–12038.
7 D. Cardenas-Morcoso, A. F. Gualdrón-Reyes, A. B. Ferreira Vitoreti, M. García-Tecedor, S. J. Yoon, M. Solis de la Fuente, I. Mora-Seró and S. Gimenez, Photocatalytic and photoelectrochemical degradation of organic compounds with all-Inorganic metal halide perovskite quantum dots, *J. Phys. Chem. Lett.*, 2019, **10**, 630–636.
8 H. Hu, M. Chen, N. Yao, L. Wu, Q. Zhong, B. Song, M. Cao and Q. Zhang, Highly stable $CsPbBr_3$ colloidal nanocrystal clusters as photocatalysts in polar solvents, *ACS Appl. Mater. Interfaces*, 2021, **13**, 4017–4025.
9 Z. Guan, Y. Wu, P. Wang, Q. Zhang, Z. Wang, Z. Zheng, Y. Liu, Y. Dai, M.-H. Whangbo and B. Huang, Perovskite photocatalyst $CsPbBr_{3-x}I_x$ with a bandgap funnel structure for $H_2$ evolution under visible light, *Appl. Catal., B*, 2019, **245**, 522–527.
10 X. Zhu, Y. Lin, J. San Martin, Y. Sun, D. Zhu and Y. Yan, Lead halide perovskites for photocatalytic organic synthesis, *Nat. Commun.*, 2019, **10**, 1–10.
11 X. Zhu, Y. Lin, Y. Sun, M. C. Beard and Y. Yan, Lead-halide perovskites for photocatalytic α-Alkylation of aldehydes, *J. Am. Chem. Soc.*, 2019, **141**, 733–738.
12 J. Wang, Y. Shi, Y. Wang and Z. Li, Rational design of metal halide perovskite nanocrystals for photocatalytic $CO_2$ reduction: recent advances, challenges, and prospects, *ACS Energy Lett.*, 2022, **7**, 2043–2059.
13 P. Chen, W.-J. Ong, Z. Shi, X. Zhao and N. Li, Pb-Based halide perovskites: recent advances in photo(electro)catalytic applications and looking beyond, *Adv. Funct. Mater.*, 2020, **30**, 1909667.
14 S. H. Teo, C. H. Ng, Y. H. Ng, A. Islam, S. Hayase and Y. H. Taufiq-Yap, Resolve deep-rooted challenges of halide perovskite for sustainable energy development and environmental remediation, *Nano Energy*, 2022, **99**, 107401.
15 H. Huang, B. Pradhan, J. Hofkens, M. B. J. Roeffaers and J. A. Steele, Solar-driven metal halide perovskite photocata-

lysis: design, stability, and performance, *ACS Energy Lett.*, 2020, **5**, 1107–1123.
16 J. T. DuBose and P. V. Kamat, Efficacy of perovskite photocatalysis: challenges to overcome, *ACS Energy Lett.*, 2022, **7**, 1994–2011.
17 J. Fu, K. Jiang, X. Qiu, J. Yu and M. Liu, Product selectivity of photocatalytic $CO_2$ reduction reactions, *Mater. Today*, 2020, **32**, 222–243.
18 D. Yan, T. Shi, Z. Zang, S. Zhao, J. Du and Y. Leng, Stable and low-threshold whispering-gallery-mode lasing from modified $CsPbBr_3$ perovskite quantum dots@$SiO_2$ sphere, *Chem. Eng. J.*, 2020, **401**, 126066.
19 Z. Hu, Z. Liu, Y. Bian, S. Li, X. Tang, J. Du, Z. Zang, M. Zhou, W. Hu, Y. Tian and Y. Leng, Enhanced two-photon-pumped emission from In situ synthesized non-blinking $CsPbBr_3/SiO_2$ nanocrystals with excellent stability, *Adv. Opt. Mater.*, 2018, **6**, 1700997.
20 Y. Tong, Q. Wang, E. Mei, X. Liang, W. Gao and W. Xiang, One-pot synthesis of $CsPbX_3$ (X = Cl, Br, I)@Zeolite: a potential material for wide–color–gamut backlit displays and upconversion emission, *Adv. Opt. Mater.*, 2021, **9**, 2100012.
21 B. Ai, C. Liu, J. Wang, J. Xie, J. Han and X. Zhao, Precipitation and optical properties of $CsPbBr_3$ quantum dots in phosphate glasses, *J. Am. Ceram. Soc.*, 2016, **99**, 2875–2877.
22 X. Huang, Q. Guo, D. Yang, X. Xiao, X. Liu, Z. Xia, F. Fan, J. Qiu and G. Dong, Reversible 3D laser printing of perovskite quantum dots inside a transparent medium, *Nat. Photonics*, 2020, **14**, 82–88.
23 S. Liu, G. Shao, L. Ding, J. Liu, W. Xiang and X. Liang, Sn-doped $CsPbBr_3$ QDs glasses with excellent stability and optical properties for WLED, *Chem. Eng. J.*, 2019, **361**, 937–944.
24 H. Zhang, X. Wang, Q. Liao, Z. Xu, H. Li, L. Zheng and H. Fu, Embedding perovskite nanocrystals into a polymer matrix for tunable luminescence probes in cell imaging, *Adv. Funct. Mater.*, 2017, **27**, 1604382.
25 Q. Zhou, Z. Bai, W. Lu, Y. Wang, B. Zou and H. Zhong, In situ fabrication of halide perovskite nanocrystal-embedded polymer composite films with enhanced photoluminescence for display backlights, *Adv. Mater.*, 2016, **28**, 9163–9168.
26 Y. Jiang, J.-F. Liao, H.-Y. Chen, H.-H. Zhang, J.-Y. Li, X.-D. Wang and D.-B. Kuang, All-solid-state Z-scheme $\alpha$-$Fe_2O_3$/Amine-RGO/$CsPbBr_3$ hybrids for visible-light-driven photocatalytic $CO_2$ reduction, *Chem*, 2020, **6**, 766–780.
27 Y. Jiang, J.-F. Liao, Y.-F. Xu, H.-Y. Chen, X.-D. Wang and D.-B. Kuang, Hierarchical $CsPbBr_3$ nanocrystal-decorated ZnO nanowire/macroporous graphene hybrids for enhancing charge separation and photocatalytic $CO_2$ reduction, *J. Mater. Chem. A*, 2019, **7**, 13762–13769.
28 X. Yue, L. Cheng, J. Fan and Q. Xiang, 2D/2D $BiVO_4$/$CsPbBr_3$ S-scheme heterojunction for photocatalytic $CO_2$ reduction: Insights into structure regulation and Fermi level modulation, *Appl. Catal., B*, 2022, **304**, 120979.
29 Y. Zhao, H. Shi, X. Hu, E. Liu and J. Fan, Fabricating $CsPbX_3$/CN heterostructures with enhanced photocatalytic activity for penicillins 6-APA degradation, *Chem. Eng. J.*, 2020, **381**, 122692.
30 Y.-H. Chen, J.-K. Ye, Y.-J. Chang, T.-W. Liu, Y.-H. Chuang, W.-R. Liu, S.-H. Liu and Y.-C. Pu, Mechanisms behind photocatalytic $CO_2$ reduction by $CsPbBr_3$ perovskite-graphene-based nanoheterostructures, *Appl. Catal., B*, 2021, **284**, 119751.
31 L. Jiao and H.-L. Jiang, Metal-organic frameworks for catalysis: Fundamentals and future prospects, *Chin. J. Catal.*, 2023, **45**, 1–5.
32 K. Sun, Y. Qian and H.-L. Jiang, Metal-Organic Frameworks for Photocatalytic Water Splitting and $CO_2$ Reduction, *Angew. Chem.*, 2023, **135**, e202217565.
33 J. Li, H. Huang, W. Xue, K. Sun, X. Song, C. Wu, L. Nie, Y. Li, C. Liu, Y. Pan, H.-L. Jiang, D. Mei and C. Zhong, Self-adaptive dual-metal-site pairs in metal-organic frameworks for selective $CO_2$ photoreduction to $CH_4$, *Nat. Catal.*, 2021, **4**, 719–729.
34 S. K. Yadav, G. K. Grandhi, D. P. Dubal, J. C. Mello, M. Otyepka, R. Zbořil, R. A. Fischer and K. Jayaramulu, Metal halide perovskite@metal–organic framework hybrids: synthesis, design, properties, and applications, *Small*, 2020, **16**, 2004891.
35 J. Hou, Z. Wang, P. Chen, V. Chen, A. K. Cheetham and L. Wang, Intermarriage of halide perovskites and metal–organic framework crystals, *Angew. Chem.*, 2020, **132**, 19602–19617.
36 C. Zhang, W. Li and L. Li, Metal halide perovskite nanocrystals in metal–organic framework host: not merely enhanced stability, *Angew. Chem.*, 2021, **133**, 7564–7577.
37 G.-Y. Qiao, D. Guan, S. Yuan, H. Rao, X. Chen, J.-A. Wang, J.-S. Qin, J.-J. Xu and J. Yu, Perovskite quantum dots encapsulated in a mesoporous metal–organic framework as synergistic photocathode materials, *J. Am. Chem. Soc.*, 2021, **143**, 14253–14260.
38 L.-Y. Wu, Y.-F. Mu, X.-X. Guo, W. Zhang, Z.-M. Zhang, M. Zhang and T.-B. Lu, Encapsulating Perovskite Quantum Dots in Iron-Based Metal–Organic Frameworks (MOFs) for Efficient Photocatalytic $CO_2$ Reduction, *Angew. Chem., Int. Ed.*, 2019, **58**, 9491–9495.
39 Z.-C. Kong, J.-F. Liao, Y.-J. Dong, Y.-F. Xu, H.-Y. Chen, D.-B. Kuang and C.-Y. Su, Core@shell $CsPbBr_3$@Zeolitic imidazolate framework nanocomposite for efficient photocatalytic $CO_2$ reduction, *ACS Energy Lett.*, 2018, **3**, 2656–2662.
40 S. Mollick, T. N. Mandal, A. Jana, S. Fajal, A. V. Desai and S. K. Ghosh, Ultrastable luminescent hybrid bromide perovskite@MOF nanocomposites for the degradation of organic pollutants in water, *ACS Appl. Nano Mater.*, 2019, **2**, 1333–1340.
41 C. Zhang, B. Wang, W. Li, S. Huang, L. Kong, Z. Li and L. Li, Conversion of invisible metal-organic frameworks to

 

luminescent perovskite nanocrystals for confidential information encryption and decryption, *Nat. Commun.*, 2017, **8**, 1138.

42 H. Tsai, H. Huang, J. Watt, C. Hou, J. Strzalka, J. Shyue, L. Wang and W. Nie, Cesium lead halide perovskite nanocrystals assembled in metal–organic frameworks for stable blue light emitting diodes, *Adv. Sci.*, 2022, **9**, 2105850.

43 H. Tsai, S. Shrestha, R. A. Vilá, W. Huang, C. Liu, C.-H. Hou, H.-H. Huang, X. Wen, M. Li, G. Wiederrecht, Y. Cui, M. Cotlet, X. Zhang, X. Ma and W. Nie, Bright and stable light-emitting diodes made with perovskite nanocrystals stabilized in metal–organic frameworks, *Nat. Photonics*, 2021, **15**, 843–849.

44 C. Peng, X. Song, J. Yin, G. Zhang and H. Fei, Intrinsic white-light-emitting metal–organic frameworks with structurally deformable secondary building units, *Angew. Chem., Int. Ed.*, 2019, **58**, 7818–7822.

45 X. Li, Y. Wu, S. Zhang, B. Cai, Y. Gu, J. Song and H. Zeng, $CsPbX_3$ Quantum Dots for Lighting and Displays: Room-Temperature Synthesis, Photoluminescence Superiorities, Underlying Origins and White Light-Emitting Diodes, *Adv. Funct. Mater.*, 2016, **26**, 2435–2445.

46 Y.-X. Tan, F.-Y. Meng, M.-C. Wu and M.-H. Zeng, Two Pb(II) dicarboxylates constructed by rigid terephthalate or flexible d(+)-camphorate with different 3D motif based on cooperative effect of steric hindrance of ligand and lone pair electrons, *J. Mol. Struct.*, 2009, **928**, 176–181.

47 B. N. Choi, J. Y. Seo, Z. An, P. J. Yoo and C.-H. Chung, An *in situ* spectroscopic study on the photochemical $CO_2$ reduction on $CsPbBr_3$ perovskite catalysts embedded in a porous copper scaffold, *Chem. Eng. J.*, 2022, **430**, 132807.

48 K. Jayaramulu, F. Geyer, A. Schneemann, Š. Kment, M. Otyepka, R. Zboril, D. Vollmer and R. A. Fischer, Hydrophobic metal–organic frameworks, *Adv. Mater.*, 2019, **31**, 1900820.

49 J. Cao, C. Yan, C. Luo, W. Li, X. Zeng, Z. Xu, X. Fu, Q. Wang, X. Chu, H. Huang, X. Zhao, J. Lu and W. Yang, Cryogenic–temperature thermodynamically suppressed and strongly confined $CsPbBr_3$ quantum dots for deeply blue light–emitting diodes, *Adv. Opt. Mater.*, 2021, **9**, 2100300.

50 X. Chen, Y. Yu, C. Yang, J. Yin, X. Song, J. Li and H. Fei, Fabrication of robust and porous lead chloride-based metal–organic frameworks toward a selective and sensitive smart $NH_3$ sensor, *ACS Appl. Mater. Interfaces*, 2021, **13**, 52765–52774.

51 B. Xu, Z. Gao, S. Yang, H. Sun, L. Song, Y. Li, W. Zhang, X. Sun, Z. Wang, X. Wang and X. Meng, Multicolor random lasers based on perovskite quantum dots embedded in intrinsic Pb–MOFs, *J. Phys. Chem. C*, 2021, **125**, 25757–25764.

52 M. Thommes, K. Kaneko, A. V. Neimark, J. P. Olivier, F. Rodriguez-Reinoso, J. Rouquerol and K. S. W. Sing, Physisorption of gases, with special reference to the evaluation of surface area and pore size distribution (IUPAC Technical Report), *Pure Appl. Chem.*, 2015, **87**, 1051–1069.

53 L. Feng, S. Yuan, L.-L. Zhang, K. Tan, J.-L. Li, A. Kirchon, L.-M. Liu, P. Zhang, Y. Han, Y. J. Chabal and H.-C. Zhou, Creating hierarchical pores by controlled linker thermolysis in multivariate metal–organic frameworks, *J. Am. Chem. Soc.*, 2018, **140**, 2363–2372.

54 K. Cheng, F. Svec, Y. Lv and T. Tan, Hierarchical micro–and mesoporous Zn–based metal–organic frameworks templated by hydrogels: their use for enzyme immobilization and catalysis of knoevenagel reaction, *Small*, 2019, **15**, 1902927.

55 G. Cai, X. Ma, M. Kassymova, K. Sun, M. Ding and H.-L. Jiang, Large-scale production of hierarchically porous metal–organic frameworks by a reflux-Assisted post-synthetic ligand substitution strategy, *ACS Cent. Sci.*, 2021, **7**, 1434–1440.

56 L. Feng, K.-Y. Wang, X.-L. Lv, T.-H. Yan and H.-C. Zhou, Hierarchically porous metal–organic frameworks: synthetic strategies and applications, *Natl. Sci. Rev.*, 2020, **7**, 1743–1758.

57 R. Xu, Q. Ji, P. Zhao, M. Jian, C. Xiang, C. Hu, G. Zhang, C. Tang, R. Liu, X. Zhang and J. Qu, Hierarchically porous UiO-66 with tunable mesopores and oxygen vacancies for enhanced arsenic removal, *J. Mater. Chem. A*, 2020, **8**, 7870–7879.

58 F. Lei, Y. Sun, K. Liu, S. Gao, L. Liang, B. Pan and Y. Xie, Oxygen vacancies confined in ultrathin indium oxide porous sheets for promoted visible-light water splitting, *J. Am. Chem. Soc.*, 2014, **136**, 6826–6829.

59 S.-Y. Kim, A.-R. Kim, J. W. Yoon, H.-J. Kim and Y.-S. Bae, Creation of mesoporous defects in a microporous metal-organic framework by an acetic acid-fragmented linker co-assembly and its remarkable effects on methane uptake, *Chem. Eng. J.*, 2018, **335**, 94–100.

60 Y. Mao, D. Chen, P. Hu, Y. Guo, Y. Ying, W. Ying and X. Peng, Hierarchical mesoporous metal–organic frameworks for enhanced $CO_2$ capture, *Chem. – Eur. J.*, 2015, **21**, 15127–15132.

61 S. Zhang, M. Du, Z. Xing, Z. Li, K. Pan and W. Zhou, Defect-rich and electron-rich mesoporous Ti-MOFs based $NH_2$-MIL-125 (Ti)@$ZnIn_2S_4$/CdS hierarchical tandem heterojunctions with improved charge separation and enhanced solar-driven photocatalytic performance, *Appl. Catal., B*, 2020, **262**, 118202.

62 M. Dong, J. Zhou, J. Zhong, H. Li, C. Sun, Y. Han, J. Kou, Z. Kang, X. Wang and Z. Su, $CO_2$ dominated bifunctional catalytic sites for efficient industrial exhaust conversion, *Adv. Funct. Mater.*, 2022, **32**, 2110136.

63 H. Guo, S. Wan, Y. Wang, W. Ma, Q. Zhong and J. Ding, Enhanced photocatalytic $CO_2$ reduction over direct Z-scheme $NiTiO_3$/g-$C_3N_4$ nanocomposite promoted by efficient interfacial charge transfer, *Chem. Eng. J.*, 2021, **412**, 128646.

64 M. Zhang, M. Lu, Z. Lang, J. Liu, M. Liu, J. Chang, L. Li, L. Shang, M. Wang, S. Li and Y. Lan, Semiconductor/Covalent–Organic–Framework Z–Scheme Heterojunctions

for Artificial Photosynthesis, *Angew. Chem., Int. Ed.*, 2020, **59**, 6500–6506.
65 V. K. Ravi, R. A. Scheidt, A. Nag, M. Kuno and P. V. Kamat, To exchange or not to exchange. suppressing anion exchange in cesium lead halide perovskites with $PbSO_4$–oleate capping, *ACS Energy Lett.*, 2018, **3**, 1049–1055.
66 L. Xie, M. Xu, X. Liu, M. Zhao and J. Li, Hydrophobic metal–organic frameworks: assessment, construction, and diverse applications, *Adv. Sci.*, 2020, **7**, 1901758.
67 A. Li, Q. Cao, G. Zhou, B. V. K. J. Schmidt, W. Zhu, X. Yuan, H. Huo, J. Gong and M. Antonietti, Three-Phase Photocatalysis for the Enhanced Selectivity and Activity of $CO_2$ Reduction on a Hydrophobic Surface, *Angew. Chem., Int. Ed.*, 2019, **58**, 14549–14555.
68 Y. Zheng, H. Yao, R. Di, Z. Xiang, Q. Wang, F. Lu, Y. Li, G. Yang, Q. Ma and Z. Zhang, Water coordinated on Cu(I)-based catalysts is the oxygen source in $CO_2$ reduction to CO, *Nat. Commun.*, 2022, **13**, 2577.